Sensors and Materials, Vol. 14, No. 1 (2002) 035–045
MYU Tokyo

S & M 0468

Tunable InP-Based Microcavity Devices for Optical Communication Systems

Jürgen Daleiden*, Nicolae Chitica and Martin Strassner

Royal Institute of Technology, Electrum 229, S-16440 Kista, Sweden

(Received May 10, 2001; accepted September 14, 2001)

Key words: optical MEMS, tunable, optoelectronic, InP, filter

Continuously tunable microcavity devices based on III/V semiconductors are key elements for future dynamic wavelength division multiplexing (WDM) systems. In this paper we present technological aspects as well as device results of surface micromachined InP-based tunable Fabry-Perot (FP) filters. Using air-gap technology and electrostatic actuation we achieve a wavelength selectivity of 0.5 nm full-width at half maximum (FWHM) for the multi-air-gap devices. The entire tuning range is 62 nm for an actuation voltage of 14 V. Single air-gap devices with solid Bragg mirrors show similar tuning characteristics and inferior values in terms of wavelength selectivity (FWHM = 10 nm). However, these devices are well suited for the monolithic integration of a photodetector.

1. Introduction

Optical fiber communication using wavelength division multiplexing (WDM) is currently being investigated to enable ultrahigh-capacity transmission.[1,2] Today's static WDM systems are becoming the leading technology for point-to-point transmission. Future trends will lead to dynamic WDM technology which will improve the functionality and flexibility of these systems.[3] Tunable devices such as optical filters and highly selective photodetectors, as well as lasers, are considered to be key elements for dynamic WDM systems.

Micromechanical devices are perfectly suited to achieve continuous tunability over a wide range. Si-based micromechanical devices are already commercially available. However, III/V-based micromechanics (GaAs, InP) are still in the research and development stage. Micromechanically tunable GaAs-based structures have been available since

*Current address: Institute of Microstructure Technologies and Analytics, Heinrich-Plett-Strasse 40, D-34132 Kassel, Germany, email:daleiden@uni-kassel.de

1995. Fabry-Perot (FP) filters,[4,5] highly selective photodetectors[6,7] and vertical cavity surface emitting lasers (VCSELs)[8–10] have been realized. More recently, InP-based micromechanics have been investigated.[11–16] The main reason for using InP is the fact that the above-mentioned WDM transmission takes place in the second (λ = 1300 nm) or third (λ = 1550 nm) communication window where the currently employed fibers have absorption minima. InP-based active optoelectronic devices are compatible with these wavelength regimes.

In assition to this there are some important advantages of III/V compound semiconductors as compared to silicon for the fabrication of optical MEMS. The epitaxial growth of, for example, $Ga_xIn_{(1-x)}As_yP_{(1-y)}$ layers on InP allows excellent stress control by varying the parameters x and y. In addition, sharp interfaces and monolayer control are provided by the epitaxy of III/V compound heterostructures. Sacrificial layers, e.g., $Ga_{0.53}In_{0.47}As$, can be etched with infinite selectivity to InP, and thus smooth interfaces with high optical quality are achieved.

In this paper we focus on InP-based optical MEMS fabricated by surface micromachining. Results of bulk micromachined InP based devices such as tunable FP filters integrated with photodetectors have been published elsewhere.[14]

2. Methods and Materials for Micromechanically Tunable Optical Devices

The basis for all wavelength tunable devices discussed in this paper is the change of the cavity length in an optical FP resonator. This implies that at least one mirror of the FP resonator is movable with respect to the other one. Thus the moving mirror is placed on top of a movable membrane or the mirror itself forms the membrane.

2.1 *Micromachining*

Two general techniques are used for fabricating the membrane: bulk micromachining and surface micromachining. In bulk micromachining the substrate underneath the device is removed by anisotropic wet or dry etching to an etch stop layer, which prevents the membrane from being etched (Fig.1, right). In the case of surface micromachining, the membrane layer(s) are on top of a sacrificial layer which is selectively removed by wet etching (Fig. 1, left).

In the actual work we concentrate on the surface micromachining of InP based devices. In this case InP is used as the membrane layer and $Ga_{0.53}In_{0.47}As$ as the sacrificial layer. The InP membranes are laterally defined by $CH_4/H_2/Ar$ reactive ion etching (RIE). In this processing step both layers, the InP membrane layer and the $Ga_{0.53}In_{0.47}As$ sacrificial layer,

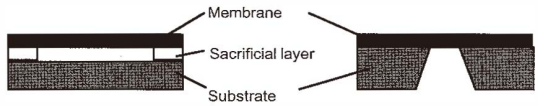

Fig. 1. Schematic illustration of the fabrication of movable membranes by surface and bulk micromachining.

are etched nonselectively and anisotropically. The result is a mesa structure with smooth steep sidewalls. Subsequently the sacrificial $Ga_{0.53}In_{0.47}As$ layer is removed by $FeCl_3/H_2O$ wet etching whereby the selectivity to InP is infinite. However, the lateral etching shows an anisotropy which has to be taken into account for the design of the devices. Figure 2 illustrates an H-shaped InP membrane which is not fully underetched. The light parts of the membrane are underetched whereas the dark parts surrounded by the dotted line are not underetched. The holding pads which are located leftmost and rightmost to the H-shaped bridge will act as the suspension after the full underetching of the membrane. The etch rate in <110> crystalline directions is 0.25 μm/min, whereas the etch rate in <100> is 1 μm/min.

After etching the sacrificial layer the sample has to be dried in such a way that the capillary forces are minimized. Otherwise, the released parts tend to collapse and stick together. CO_2 critical point drying gives excellent results.[17] InP membranes with dimensions of 0.37 μm, 20 μm and 100 μm (thickness, width, length) with air gaps of 0.38 μm have been suspended without sticking problems.

2.2 *Stress control*

Precise control of the stress in the suspended layers is essential for the successful fabrication of micromachined devices. Generally the overall stress in a layer can be described by a gradient part σ_{grad} and a homogeneous part σ_{hom}.

The test structures used to measure the internal stress gradients of the films consist of a set of suspended cantilevers fixed to the substrate at one end (reference plate). An internal stress gradient will deflect the cantilever beam tip and the deflection can be measured as the height of the tip above the reference plate. The stress gradient σ_{grad} can be calculated from the cantilever tip deflection d according to the following formula:[18]

$$\frac{d\sigma_{grad}}{dx} = \frac{E}{1-\nu}\frac{2}{l^2}\delta, \tag{1}$$

where σ_{grad} is the internal stress gradient, x the thickness of the layer, E the elastic modulus

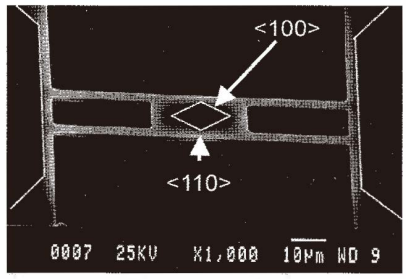

Fig. 2. H-shaped InP membrane. The light parts of the membrane are underetched. The dark parts surrounded by the dotted line are not underetched. The image shows the lateral anisotropy of this etching step. The etch rate in <100> is four times higher than in <110>.

of the beam (E_{InP}=61 GPa), ν Poisson's ratio (ν_{InP}=0.357),[19] and l the length of the cantilever and d the cantilever tip deflection.

For the characterization of the homogeneous stress, the structure shown in Fig. 3 has been used. It consists of two essentially symmetrical halves, each with two actuator beams and one indicator. One end of each actuator beam is fixed to the substrate by a holding pad and the other is connected to the indicator by a narrow hinge. When the actuator beams are released in the sacrificial layer etch, a homogeneous stress causes elongation or contraction. The actuator beams are not directly opposite to each other at the connection to the indicator, but are slightly separated. Thus a torque is created that deflects the indicator. The magnitude of the deflection corresponds to the magnitude of the internal homogeneous stress, and its direction corresponds to the type of stress, i.e., tensile or compressive stress. A tensile homogeneous stress causes a contraction of the actuator beams. Consequently, the indicators rotate counterclockwise. Compressive stress forces the indicator to rotate clockwise. The sensitivity is doubled by placing pairs of devices opposite each other.

The homogeneous stress can be determined according to the formula[18]

$$\sigma_{hom} = \frac{E}{1-\nu}\frac{d}{2l_a l_i}\delta, \tag{2}$$

where σ_{hom} is the internal homogeneous stress, E the elastic modulus, ν Poisson's ratio (ν_{InP}=0.357) , d the distance between the anchor of the actuator beam and the center of rotation, l_a the length of the actuator beam, l_i the length of the indicator beam, and δ the deflection.

It has been observed that InP layers grown by metal organic vapor phase epitaxy (MOVPE) contain arsenic as an impurity whenever they are grown after an As-containing layer.[20] This results in InP cantilevers that bend upwards due to stress caused by a gradient in the As distribution in the InP layer. The homogeneous stress in these structures is compressive, causing the InP bridge structures to buckle.

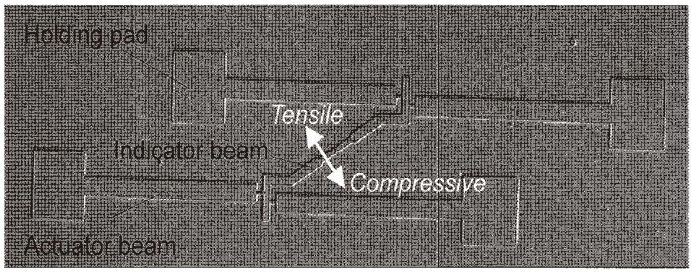

Fig. 3. Test structures for homogeneous stress characterization. The four quadratic holding pads are not underetched while the rest of the structure is underetched. According to the value of the stress the actuator beams expand or contract, causing the indicators to rotate clockwise (compressive) or counterclockwise (tensile).

This problem can be solved by either optimizing the MOVPE growth procedure[17] or replacing InP with $Ga_xIn_{1-x}As_yP_{1-y}$ with a minimum stress gradient and a slight tensile homogeneous stress.[20]

2.3 *Actuation*

Both thermal and electrostatic actuation is possible. In the subsequent studies the membranes are electrostatically actuated. The p-doped membrane layer, the intrinsic sacrificial layer and the n-doped substrate form a p-i-n structure. By reverse biasing the p-i-n diode, the suspended membrane moves toward the substrate. The advantage of this principle is the low actuation power due to the low leakage current. The p-i-n structure can be designed for a high breakdown voltage, allowing for a low power dissipation under a large actuation voltage.

Figure 4 shows a schematic diagram of a tunable FP filter comprising two distributed Bragg reflectors (DBRs) separated by an air cavity. The upper DBR is p-doped and the lower DBR is n-doped. The arrows in the top part of the diagram schematically show five channels of a WDM system which are coupled to the filter. The air gap (thickness L) is designed to select the channel with the longest wavelength (e.g., $\lambda_1=L$) in the nontuned case (Fig. 4, left). By reverse biasing the structure the suspended upper DBR will move towards the lower DBR due to electrostatic forces (Fig. 4, right). Thereby, the length of the cavity is reduced and consequently channels with shorter wavelength ($\lambda_2=L-\Delta L$) are transmitted. The actuated DBR is preferably a circular membrane suspended by thin stripes. Thus the central circular area remains flat under actuation.

3. Device Results

In this section we describe tunable InP-based microcavity devices. We present two different tunable FP filters specified as an "all air-gap filter" and a "mixed filter."

3.1 *All air-gap filter*

Figure 5 shows the vertical structure of the device.[13] The sequence of the epitaxial

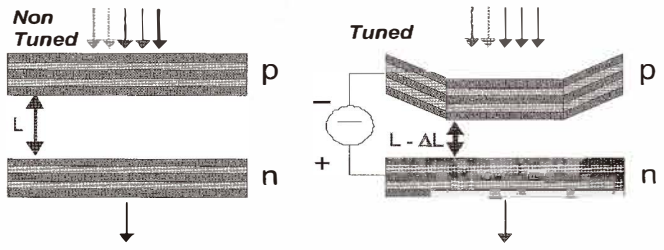

Fig. 4. Schematic diagram of the FP filter. Tuning is achieved by capacitive actuation of the upper DBR.

layers is an alternation between $Ga_{0.53}In_{0.47}As$ (sacrificial layers) and InP (membrane layers). In this design the function of the air layers is twofold:

1. High refractive index in contrast to InP suspended layers
2. Tuning capability for the air cavity

The air-gap cavity (layer 6 from the top) is defined between the two high reflectivity InP/air-gap DBR mirrors. With our design a calculated reflectivity of 99.7% is reached with only 2.5 periods of InP/air. The cavity length is $\lambda/2$ (λ = 1550 nm), resulting in a high tuning efficiency and a large free spectral range (FSR) of the FP filter. The layers belonging to the top DBR are p-doped and the layers of the bottom DBR are n-doped. By applying a reverse bias between the two stacks, the two InP layers which are adjacent to the air cavity attract each other and thereby reduce the air cavity length. Consequently the filter resonance is shifted to shorter wavelengths.

Figure 6 shows a scanning electron micrograph of the device. The circular filter membranes have a diameter of 40 μm and are each suspended by two 10-μm-wide beams each. The lengths of the beams vary between 10 μm and 100 μm. The beams are fixed to the substrate by the quadratic holding pads which are not underetched. The contact of the

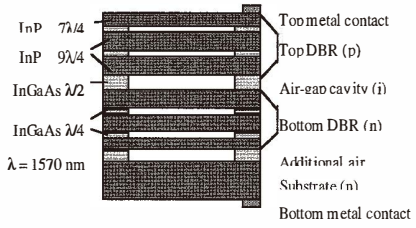

Fig. 5. Schematic cross-sectional view of the tunable "all air-gap" filter. The DBR mirrors consist of three suspended InP layers separated by air gaps ($\lambda/4$). The air cavity has an optical length of $\lambda/2$.

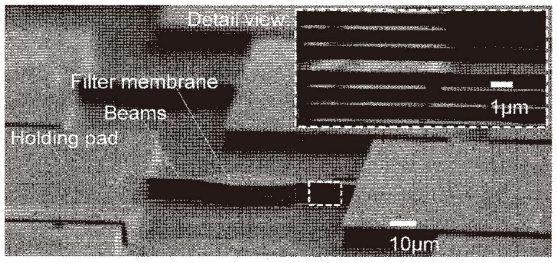

Fig. 6. Scanning electron micrograph of the tunable "all air-gap" filter. The circular filter membranes are each suspended by two 10-μm-wide beams. The beams are fixed to the substrate by the quadratic holding pads which are not underetched. The contact of the p-doped layers is positioned on top of the holding pads.

p-doped layers is positioned on top of the holding pads.

For the characterization of the spectral transmission, the amplified spontaneous emission of an erbium-doped fiber amplifier (EDFA) was coupled to the filter via a lensed fiber. The transmitted signal was collected from the back side of the chip with a gradient index (GRIN) lensed fiber and characterized by an optical spectrum analyzer.

A typical transmission spectrum of the filter is presented in Fig. 7. The FWHM of the device is approximately 0.5 nm with an insertion loss of –3dB. The inset shows the tuning characteristic of the filter. The measured data points follow with good approximation a square dependence of the resonance wavelength on the bias voltage. This dependence is characteristic of an electrostatic actuation. The maximum tuning range of the filter is $\Delta\lambda$ = 62 nm for an actuation voltage of 14 V.

3.2 *Mixed filter*

This design aims primarily for a device that is simple, robust and easily integratable with an InGaAsP/InP based photodetector.[12,21] Figure 8 shows schematically the vertical structure of the device. The top dielectric DBR is placed on a micromechanically moveable bridge. By electrostatic actuation of the bridge, the length of the air-gap cavity defined between the two reflectors can be adjusted and the resonance wavelength is tuned.

The filter has been designed for a FWHM of 10 nm, meeting the requirements for coarse WDM for optical interconnects. The top reflector consists of a stack of $Si/SiO_2/Si/SiN_x$ $\lambda/4$ layers on top of the 7/4 λ InP bridge, whereas the bottom reflector comprises 20 pairs of $InP/Ga_{0.36}In_{0.64}As_{0.77}P_{0.23}$ $\lambda/4$ layers. The cavity consists of a 1 λ air-gap and a $\lambda/2$ InP layer providing for the integration of an active region in a future resonant cavity

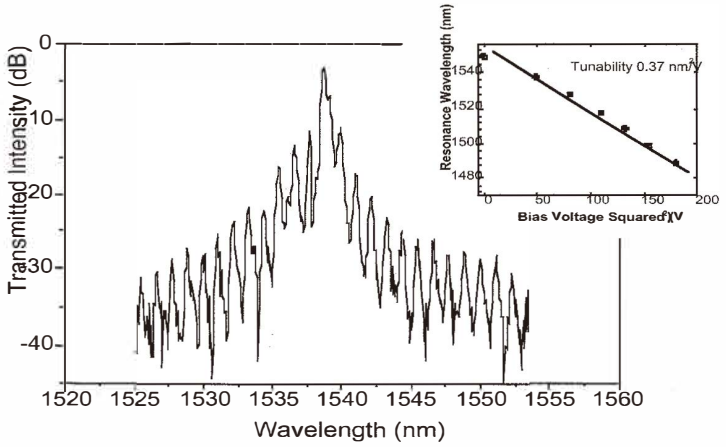

Fig. 7. Transmission spectrum of the "all air-gap" filter. *Inset:* Tuning characteristic of the filter. The fitted line corresponds to a quadratic dependence of the tuning on the applied bias.

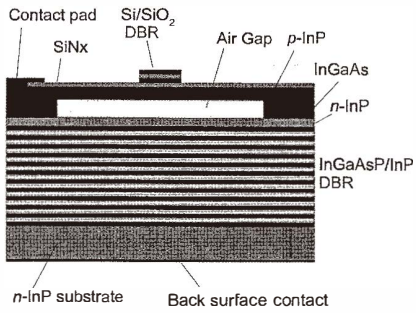

Fig. 8. Schematic cross-sectional view of the tunable "mixed" FP filter.

detector. The effective length of the FP resonant cavity is estimated to be 2.7 λ.

Figure 9 shows a scanning electron micrograph of the finished device. The I-V characteristics of the fabricated structures indicate a breakdown voltage of more than 40 V and a low leakage current of typically less than 10 μA at a reverse bias of 30° V. The low leakage current obtained for the relatively large area structures (more than 200×300 μm^2) implies that the p-i-n structures are of good quality. The low leakage current provides for a low actuation power.

The optical characteristics of the filters were evaluated by microreflectivity measurements in a spot 15 μm in diameter centered on the top DBR. A collimated white light beam at normal incidence was used for the measurements. The tuning characteristics of the filters was measured by recording the reflectance spectra corresponding to different values of applied bias. Typical resonance characteristics of the FP filter are presented in Fig. 10. The FWHM of the resonance dip is 10° nm. Figure 11 shows the tuning characteristics of the filters corresponding to different lateral designs (Fig. 11, inset).

Maximum tuning values of $\Delta\lambda = 62$ nm with 13 V actuation voltage have been achieved with the most flexible structures (H170).

The relatively rigid structures ("I 80 and I 110") have a calculated natural resonance frequency on the order of 1 MHz[22] and are less sensitive to external perturbations such as vibrations and shocks. The penalty is the higher actuation voltage required for a particular tuning. If a lower actuation voltage is the primary requirement the more flexible structures are preferable.

4. Summary and Conclusions

We have presented two different types of InP-based tunable FP filters specified as an "all air-gap filter" and a "mixed filter." The former type shows superior performance in terms of filter selectivity. Due to the high finess DBRs, the " all air-gap" filter shows a FWHM of 0.5 nm. The maximum tuning range is $\Delta\lambda = 62$ nm for an actuation voltage of 14 V.

However, the "mixed filter" has advantages for the future monolithic integration of a

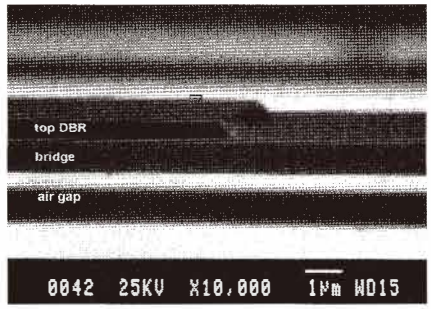

Fig. 9. Scanning electron micrograph of the filter. The dielectric DBR is placed on top of the suspended electrostatically movable bridge.

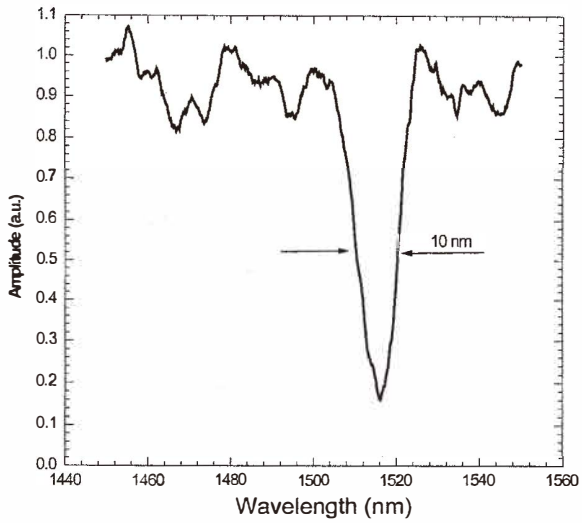

Fig. 10. Typical resonance characteristics of the FP filter. The reflectivity spectrum was recorded with a collimated beam and a spot size 15 μm in diameter.

resonant cavity photodetector. The InP layer located inside the cavity provides for the integration of an active region. This layer is easier to access for electrical contact than in the multi air-gap device.

The devices presented in this work were fabricated by surface micromachining. This process has the advantage that it is compatible with standard semiconductor mass production. High-performance tunable filters and integrated photodetectors are achieved by InP

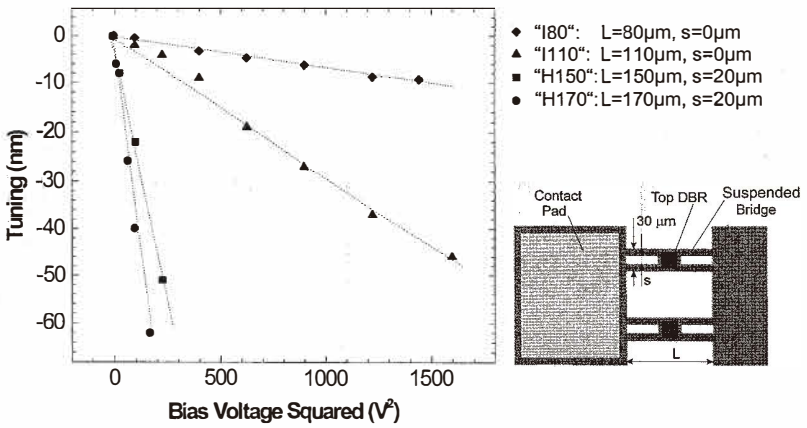

Fig. 11. Tuning characteristics of the fabricated filters. The data sets correspond to filters with different micromechanical structures (see inset). The fitted lines correspond to a quadratic dependence of the tuning on the applied bias, characteristic to an electrostatic actuation.

bulk micromachining.[14] This two-chip technology allows the optimization of the electrical properties of the photodiode (chip 1) and the micromachined actuators (chip 2) separately. However, the alignment of the two chips is critical and difficult to integrate in production.

Generally, InP-based optical MEMS have a high potential in terms of multifunctional devices for optical communication systems such as widely tunable highly selective filters, photodetectors and VCSELs.

Acknowledgement

This work has been funded in the frame of the European ESPRIT project MOEMS. The fruitful collaboration of all participants of this project is acknowledged. In particular we would like to thank P. Viktorovitch, J. L. Leclercq, and A. Spisser for their close cooperation. The support of H. Hillmer is expressly acknowledged.

References

1 J. M. Senior, M.R. Handley and M.S. Leeson: IEEE Communications Magazine (December 1998) p. 28.
2 P. Green: IEEE Communications Magazine (January 2001) p. 54.
3 D. Sadot and E. Boimovich, IEEE Communications Magazine (December 1998) p. 50.
4 E. C. Vail, M.S. Wu, G. S. Li, L. Eng and C. J. Chang-Hasnain: Elect. Lett. **31** (1995) 228.
5 P. Tayebati, P. D. Wang, D. Vakhshoori and R. N. Sacks: IEEE Photonics Technol. Lett. **10** (1998) 394.

6 S. Strite and M.S. Ünlü: Electron. Lett. **31** (1995) 672.
7 G. L. Christenson, A. T. T. D. Tran, Z. H. Zhu, Y. H. Lo, M. Hong, J. P. Mannaerts and R. Bhat: IEEE Photonics Technol. Lett. **9** (1997) 724.
8 M. C. Larson and J. S. Harris, Jr.: Appl. Phys. Lett. **68** (1996) 891.
9 F. Sugihwo, M.C. Larson and J.S. Harris, Jr.: Appl. Phys. Lett. **72** (1998) 10.
10 C. Chang-Hasnain: IEEE Journal on Selected Topics in Quantum Eletctronics **6** (2000) 978.
11 A. Spisser, R. Ledantec, C. Seassal, J.L. Leclercq, T. Benyattou, D. Rondi, R. Blondeau, G. Guillot and P. Viktorovitch: IEEE Photonics Technol. Lett. **10** (1998) 1259.
12 N. Chitica, J. Daleiden, M. Strassner and K. Streubel: IEEE Photonics Technol. Lett. **11** (1999) 584.
13 J. Daleiden, N. Chitica, M. Strassner, D. Rondi, E. Goutain, J. Peerlings, J. Pfeiffer, R. Riemenschneider, K. Hjort, R. Dantec, T. Benyattou, A. Spisser, J. L. Leclerq and P. Viktorovitch: Proceedings of the Int. Conf. on InP and Rel. Mat. (1999) p.285.
14 J. Peerlings, R. Riemenschneider, V. Naveen Kumar, M. Strassner, J. Pfeiffer, V. Scheuer, J. Daleiden, K. Mutamba, S. Herbst, H. L. Hartnagel and P. Meissner: IEEE Photonics Technology Letters **11,** No.2 (1999).
15 D. Vakhshoori, P. Tayebati, C.-C. Lu, M. Azimi, P. Wang, J.-H. Zhou and E. Canoglu, Electron. Lett. **35** (1999) 1.
16 V. Jayaraman, T. J. Goodnough, T. l. Beam, F. M. Ahedo and R. A. Maurice: IEEE Photon. Technol. Lett. **12** (2000) 1595.
17 P. Viktorovitch, J. L. Leclercq, E. Goutain and D. Rondi: SPIE Microfabrication Symposium Santa Clara CA (2000)
18 F. Ericson, S. Greek, J. Söderquist, J.-A. Schweitz and J. Micromech: Microeng. **7** (1997) 30.
19 S. Greek and N. Chitica: Sensors and Actuators A **78** (1999) 1.
20 N. Chitica, M. Strassner and J. Daleiden: Appl. Phys. Lett. **77** (2000) 202.
21 M. Strassner, J. Daleiden, N. Chitica, D. Keiper, B. Stålnacke, S. Greek and K. Hjort: Sensors and Actuators A **85** (2000) 249.
22 S. Greek, R. Gupta and K. Hjort: IEEE J. Microelectromech. Syst. **8** (1999) 328.